

Absorption, Adsorption, and Desorption Studies of the Oxygen/Rh(111) System Using O₂, NO, and NO₂

Kevin A. Peterlinz[†] and Steven J. Sibener*

James Franck Institute and The Department of Chemistry, The University of Chicago, 5640 South Ellis Avenue, Chicago, Illinois 60637

Received: July 8, 1994; In Final Form: October 12, 1994[⊗]

The adsorption of oxygen on the Rh(111) surface using O₂, NO, and NO₂ has been studied using thermal desorption of O₂, helium diffraction, and time-resolved specular helium scattering. At all surface temperatures, T_s , the surface coverage of oxygen saturates with $\theta_{\text{O}}(\text{sat}) = 0.5$ ML (monolayers). At $T_s > 375$ K, additional subsurface oxygen is absorbed. The subsurface O will segregate to and desorb from the Rh(111) surface at $T_s > 650$ K. The rate of subsurface deposition varies with the source of O, with $\text{NO}_2 \gg \text{NO} > \text{O}_2$. For absorption of O, $E_a = 4.3 \pm 0.7$ kcal/mol. The difference in enthalpy between the surface and subsurface O is 4.3 ± 0.3 kcal/mol. For $\theta_{\text{O}} < 0.15$ ML, O₂ desorption occurs with second order kinetics, with $E_a = 56 \pm 2$ kcal/mol. The shape of O₂ desorption peaks at total (surface + subsurface) O ~ 0.5 ML is independent of the source of O, surface or subsurface. Rate analysis indicates that the interatomic interactions between coadsorbed O species are approximately the same magnitude as the interactions between adsorbed and absorbed O species.

I. Introduction

Oxygen adsorption on noble metal surfaces has been extensively studied in the past due to the extensive use of these metals in automobile catalytic converters. Oxygen adsorbs and reacts with harmful CO emissions to produce the much less harmful CO₂. In these catalytic reactions, dissociative adsorption of O₂,¹ NO,² and NO₂ can be sources of reactive O on the catalytic surface. On single-crystal fcc (111) surfaces, the saturation coverage of O from low pressures ($< 10^{-3}$ Torr) of O₂ and low surface temperatures ($T_s < 400$ K) is known to produce a saturation coverage ($\theta_{\text{O}}(\text{sat})$) of 0.25 monolayers (ML) on Pt(111)^{3–5} and Pd(111),^{5–7} 1.4 ML on Ru(001),⁸ and 0.50 ML on Rh(111).⁹ $\theta_{\text{O}}(\text{sat})$ from NO dissociation at low surface temperatures ($T_s < 325$ K) is always less.^{3,10}

Experiments at higher pressures and temperatures have produced both higher $\theta_{\text{O}}(\text{sat})$ ^{11,12} and epitaxial layers of the metal oxide species.¹³ More recent work has shown that NO₂ is much more efficient than O₂ (at similar pressures and surface temperatures) at depositing O on these surfaces. The saturation coverage of O on Pt(111) was increased to 0.75 ML,^{3–5} and the saturation coverages on Pd(111)^{5–7} and Ru(001)⁸ were increased to 1.2 and 3 ML, respectively, with subsequent amounts of adsorbed O absorbing into the subsurface region. Thiel et al.¹⁴ reported evidence for O penetration from Rh(111) into the bulk for $T_s > 390$ K. The existence of subsurface O species has been shown to affect CO oxidation reactions on several surfaces.^{15,16} Very few studies exist, however, for which O deposition is studied at CO oxidation temperatures ($T_s = 400$ – 650 K) and none in which the kinetics of deposition are studied in detail.

We present here a study of O deposition on Rh(111) using O₂, NO, and NO₂. Using O₂ and NO, we show that the maximum deposition of O from each at $T_s > 400$ K is much greater than 0.50 ML. Using a combination of thermal programmed desorption (TPD), time-resolved specular He

scattering, and He diffraction, we show that almost all the O in excess of 0.50 ML is absorbed into the subsurface region. Using both absorption rate and equilibrium coverage measurements, we determine the difference in enthalpy between the surface and subsurface oxygen species. From time-resolved specular He scattering measurements, we determine the low-coverage ($\theta_{\text{O}} < 0.20$ ML) O₂ desorption rates and activation energies. Finally, we interpret the line shape of higher coverage O₂ TPDs in terms of the O–O interactions both on the surface and between surface and subsurface species.

II. Experimental Section

The apparatus, described elsewhere,^{17,18} consists of a three molecular-beam source, a UHV chamber with a rotatable quadrupole mass spectrometer, and the controlling computer system. The molecular-beam source contains three quadruply differentially pumped molecular beams horizontally coplanar and aligned and collimated to a single scattering center in the UHV chamber. Each beam has a computer-controlled beam shutter, and the center He beam, axially 15° from both side beams, has a 10–400 Hz chopper 21.21 cm from the scattering center. The O₂, NO, and CO side beams were run with a backing pressure of 760 Torr. The NO₂ side beam was run at 298 K. The center He beam was an ultra-high-purity (UHP) grade (Linde) He. The UHV chamber contained the Rh(111) crystal, oriented to within 0.5°, on a fully rotatable mount which also allowed for 140° azimuthal rotation and tilting of the crystal about the scattering plane.

The UHV chamber, pumped with a 400 L/s ion pump, also contains an Auger–sputter gun assembly that is moved under the crystal for argon ion sputtering and Auger spectroscopy. The quadrupole mass spectrometer, with an electron bombardment ionizer 14.45 cm from the scattering center, is rotatable from -5° to 135° from the three-beam plane. The crystal is rotatable from -135° to 135° from the three-beam plane. A residual gas analyzer (RGA) attached to the chamber was used to analyze background gases and to collect TPD data when the rotatable quadrupole mass spectrometer was simultaneously being used to collect He scattering data.

[†] Current address: Chemistry Department, George Washington University, 725 21st Street, N.W., Washington, DC 20052.

[⊗] Abstract published in *Advance ACS Abstracts*, February 1, 1995.

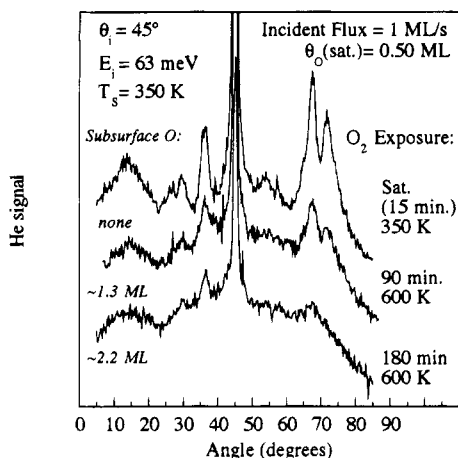


Figure 1. 45° incident He diffraction from saturated 350 K O/Rh(111). Shown here are He diffraction runs for a 45°, 63 meV He beam from a 350 K O/Rh(111) surface. The well-known saturated (0.50 ML) (2×2) O/Rh(111) overlayer has the characteristic ($1/2, 1/2$) peak at 36° (top curve). With additional exposure of O₂, the total amount of O increases to 1.8 ML (middle curve) and then to 2.7 ML (bottom curve). Note that, although the ($1/2, 1/2$) peak (as well as all of the other peaks) decreases in intensity, it does not change width or relative intensity, indicating that the same 0.50 ML (2×2) O/Rh(111) overlayer still exists on the surface. The calculated subsurface O concentrations are indicated in italics (1 ML = 1.6×10^{15} atoms/cm²).

The computer system consisted of an AST 286, with an Ortec multichannel scalar (MCS) board, interfaced to a computer-aided measurement and control (CAMAC) crate and a Eurotherm temperature controller. The computer system was used to control shutter timing, temperature, and mass spectrometer rotation as well as to collect kinetics, TPD, reflectivity, and diffraction data.

Surface preparation consisted of heating the Rh(111) crystal in 10^{-5} Torr of O₂ for 2–3 h at 500–900 K, sputtering in 5×10^{-5} Torr of argon at 3 μ A for 1.5–2 h at 500–900 K, and annealing to 1350 K. Cleanliness was checked with Auger, and cleaning procedures were repeated until S, C, and B, the only detectable contaminants, were no longer detectable. The surface temperature was maintained and measured to within 0.1 K with the Eurotherm temperature controller.

The crystal was cooled for diffraction via a liquid nitrogen cold finger electrically insulated from the resistive heating system controlled by the Eurotherm. Typically, in order to maintain 1350 K, we required a current of 40 A. For diffraction, the crystal was azimuthally oriented along the $\langle 01\bar{1} \rangle$ and $\langle 11\bar{2} \rangle$ directions to within 0.5° using He diffraction from a saturated (2×2) 0.75 ML CO overlayer. All He diffraction was done with an incident He beam which was produced by supersonic expansion of 55 psia He behind a 100 μ m pinhole. The chamber pressure rise due to this beam was typically $(3-9) \times 10^{-9}$ Torr, and the straight through (unscattered) beam has a full width at half-maximum (fwhm) of 1°.

III. Results

A. θ_0 Measurements: Understanding O₂ TPDs. 1. *O₂ TPD—He Diffraction Evidence for Subsurface O.* When low pressures ($<10^{-3}$ Torr) of O₂ are dosed onto clean Rh(111) surfaces with $T_s < 300$ K, the O/Rh(111) overlayer saturates at 0.50 ML^{9,19} (checked for this by comparison of desorbed O₂ signal with desorbed CO signal and titrated CO₂ signal²⁰). The Bragg peaks for this overlayer occur at positions consistent with a (2×2) structure^{9,19} or rotated domains of (2×1). Our He diffraction (Figures 1 and 2, saturated O) shows that, indeed,

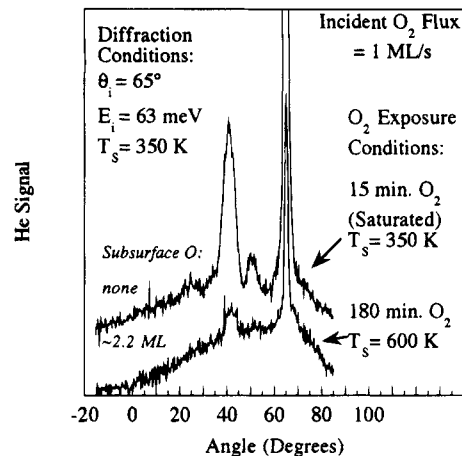


Figure 2. 65° incident He diffraction from saturated 350 K O/Rh(111). Shown here are He diffraction runs for a 65°, 63 meV He beam from a 350 K O/Rh(111) surface. Again, the well-known saturated (0.50 ML) (2×2) O/Rh(111) overlayer diffraction curve shows both half-order and first-order peaks (top curve). With additional exposure of O₂, the total amount of O increases to 2.2 ML (bottom curve). Again, note that, although the peak intensities decrease, they do not change width or relative intensity, indicating that the same 0.50 ML (2×2) O/Rh(111) overlayer still exists on the surface.

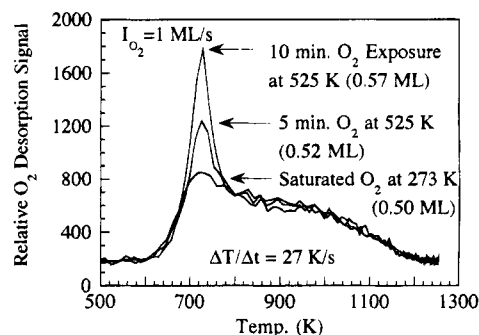


Figure 3. O₂ TPD, comparison of 273 K dosing versus 525 K dosing. Shown here are the thermal programmed desorption (TPD) spectra for O₂ desorbing from Rh(111) with a heating rate of 27 K/s. For the known saturated 0.50 ML O/Rh(111) overlayer, created by exposing the 273 K surface to a 1 ML/s 63 meV O₂ beam until saturated with O (~ 15 min), the spectra has a characteristic peak at 700 K followed by a broad peak centered at ~ 900 K. For O/Rh(111) overlayers grown by dosing O₂ onto a 525 K surface, the TPD spectra exhibit an increase in the 700 K peak intensity while the broad peak stays the same. This increase occurs only at higher surface temperatures ($T_s > 375$ K), and the peak position suggests a low binding energy O state. He diffraction data (Figures 1 and 2) indicate that $\theta_0 = 0.50$ ML for all O₂ exposures. Since the increase in O concentration is not due to increases in θ_0 , the increase in the 700 K peak is due to increased subsurface O concentration.

an overlayer structure does exist, with many half-order peaks apparent in the diffraction curve. At less than saturation coverages, diffraction has been observed only at $\theta_0 \sim 0.15-0.30$ for the O/Rh(111) (2×2) overlayer (maximized at 0.25 ML).^{9,20} Note that in this paper θ_0 refers explicitly to the concentration or coverage of surface O species at the surface–vacuum interface and that C_0 refers to the subsurface O concentration. As shown in Figure 3, we can increase the amount of O₂ which desorbs from the Rh(111) from 0.50 ML, the saturation value at $T_s = 300$ K, to higher values by dosing at $T_s = 525$ K. Similarly, we see that dosing with NO at similar beam fluxes (Figure 4) increases the rate at which we deposit the excess O.

One problem with TPD measurements in other types of UHV systems is that O is adsorbed on and thus desorbed from surfaces inside the UHV chamber other than the surface of interest. Since

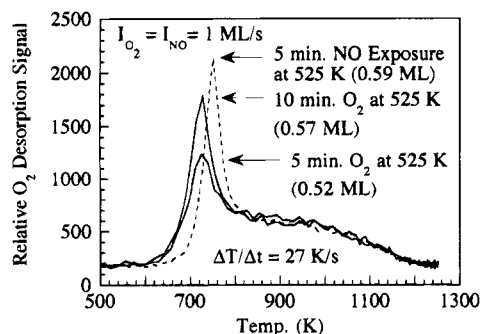


Figure 4. O_2 TPD, comparison of NO dosing versus O_2 dosing. Shown here are the thermal programmed desorption (TPD) spectra for O_2 desorbing from Rh(111) with a heating rate of 27 K/s. Dosing with NO or O_2 produces a similar TPD curve. The rate at which additional (subsurface O) is deposited, though, is much faster for NO dosing than for O_2 dosing. There is a slight shift toward higher temperature in the position of the initial, sharp peak for NO dosing as compared with O_2 dosing.

we use well-collimated beams to dose the crystal, note that we dose only a 3 mm diameter spot only on the face of the 10 mm \times 14 mm Rh(111) crystal. Our doubly differentially pumped mass spectrometer has a 1° field of view of the crystal. When the crystal was dosed and taken out of this field of view, we saw no O_2 signal from the background. Thus, we conclude that all of the O_2 desorption originated from the face of the crystal. We note that the background pressure of all gases used to dose the crystal never rose above 7×10^{-9} Torr. When the crystal was exposed to this background O_2 out of the scattering position (i.e., with no direct beam exposure) and then returned to the scattering position, we detected only 0.005 ML of O_2 desorbing from the crystal with both our differentially pumped and our background (RGA) mass spectrometers.

Since the detected O_2 desorbed from the face of the crystal, two possibilities exist. One possibility is that the O in excess of 0.50 ML is adsorbed on the face of the crystal. In this case we would expect the half-order diffraction peaks to disappear as we approached $\theta_O = 1$ ML. The other possibility is that the excess O absorbed or diffused into the subsurface region. In this case, we would expect perhaps a small perturbation on the intensities of the He diffraction signal. If this sort of incorporation of O into the Rh lattice reduces the binding energies of surface species,²¹ the diffraction signal from the adsorbate overlayer would be reduced at a given T_s due to increases in the Debye–Waller factor.^{22–24} However, we would also expect to still see the half-order peaks. We see that the results of Figure 1 indicate the latter. The peak intensities decrease, but the intensities of half-order peaks relative to the first order peaks are about the same. Thus, we conclude that there is no significant increase in the amount of surface O, and the desorbed O_2 in excess of the ~ 0.5 ML surface O must have originated from the subsurface region.

2. Measuring θ_O with He Reflectivity. As we have already shown,²⁰ time dependent He reflectivity measurements can be used to monitor θ_O over wide temperature ranges. Having previously calibrated the relationship between He reflectivity and θ_O , we used He reflectivity to measure $\theta_O(t)$ during our experiments. Figure 5a shows the He reflectivity during a CO titration experiment on the O_2 -predosed 525 K Rh(111) surface. Note that the reflectivity initially decreases and then increases for each 5 s pulse of 1 ML/s CO, indicating that CO initially adsorbs and then desorbs or reacts with adsorbed O. Up to 35 s of CO dosing time, θ_O decreases steadily, as indicated by the increase in the maximum He reflectivity during the 10 s interval between pulses for the first seven CO pulses. Subsequent TPD

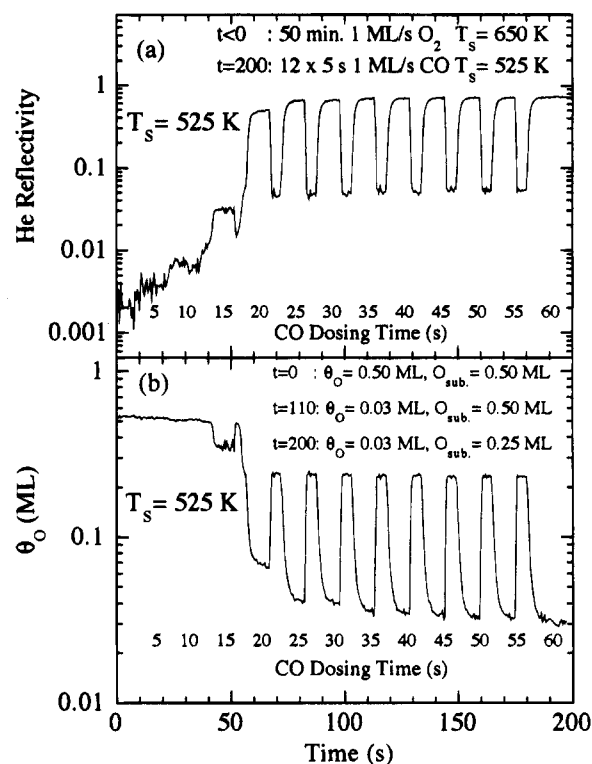


Figure 5. He reflectivity measurements of θ_O for CO titration experiment. Shown are He reflectivity measurements of θ_O made while exposing 525 K Rh(111) to 12–5 s exposures of a 1 ML/s 88 meV CO beam. The Rh(111) had been previously exposed to a 1 ML/s 88 meV O_2 beam at $T_s = 650$ K for 50 min. Panel (a) shows the He reflectivity measurements. There is a 10 s interval between the 5 s CO exposures. The He reflectivity initially decreases during the 5 s CO exposure, indicating an increase in θ_{CO} as CO adsorbs, and then the He reflectivity increases during the 10 s intervals, indicating a decrease in θ_{CO} as the CO desorbs or reacts with adsorbed O (producing CO_2). The maximum He reflectivity attained during each 10 s interval was used to determine θ_O after each CO exposure. Panel (b) shows data converted from He reflectivity to θ_O . There is a steady decrease in θ_O for the first seven CO exposures, and the minimum $\theta_O = 0.035$ ML for all CO exposures from 35 to 60 s. Subsequent TPD measurements showed that, after a 35 s CO exposure, the amount of subsurface O was 0.5 ML, and after 60 s of CO exposure, the amount of subsurface O was 0.25 ML.

measurements showed that, after a 35 s CO exposure, the amount of subsurface O was 0.5 ML, and after 60 s of CO exposure, the amount of subsurface O was 0.25 ML. We note that changes in the Debye–Waller factor for Rh(111) due to the presence of subsurface oxygen can affect the He surface reflectivity. However, we note that in Figure 5a the He reflectivity between CO pulses recovers to the same value despite a change from 0.5 to 0.25 ML for the subsurface O concentration. This result indicates that the subsurface O has an insignificant effect on the He reflectivity measurements. From the conversion of the He reflectivity to θ_O (Figure 5b), the steady state $\theta_O = 0.035$ ML after 35 s exposure to CO. Our previous calibrations²⁰ were accurate for $T_s = 450$ – 625 K for $\theta_O = 0$ – 0.50 ML. Our data fit the Comsa–Poelsema model for a disordered adsorbate²⁰ for $\theta_O < 0.15$ ML, and there was an ordered O overlayer at higher θ_O . At higher T_s , the disordered overlayer should still follow the Comsa–Poelsema model, so in subsequent measurements we use the He reflectivity calibration for $\theta_O < 0.15$ ML to determine θ_O from our He reflectivity measurements when $T_s > 625$ K.

3. θ_O versus O_2 Desorption: Where Is the O? Figure 6 confirms our He reflectivity calibration of O coverage at low coverages and high temperatures. Shown in Figure 6 are the

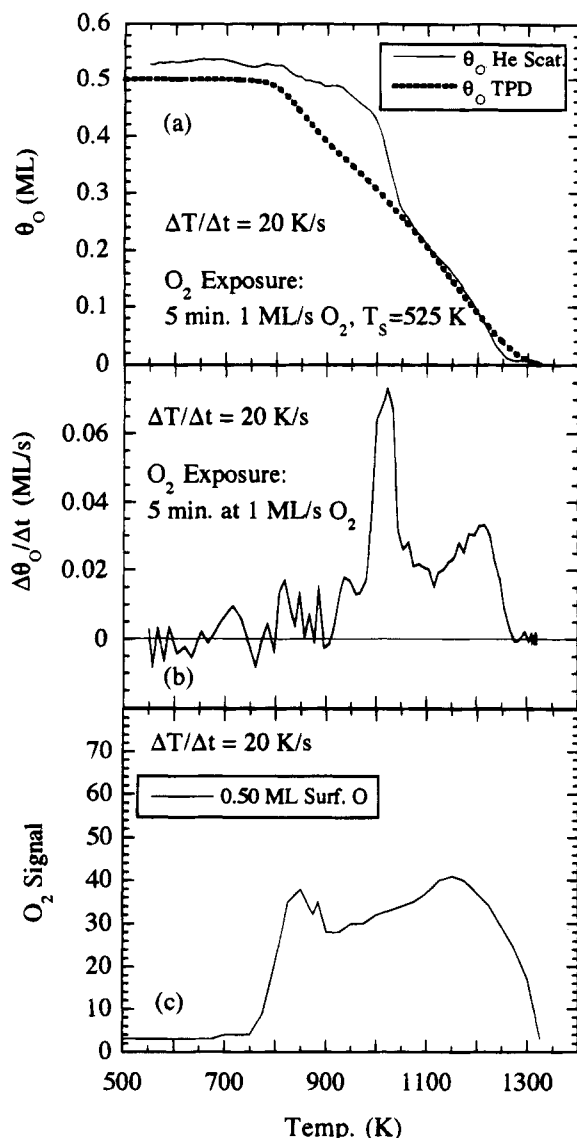


Figure 6. Confirmation of He reflectivity calibration of θ_{O} . Shown are measurements of θ_{O} and O_2 desorption made while heating Rh(111) which had been exposed to a 1 ML/s 63 meV O_2 beam at $T_{\text{S}} = 525$ K for 5 min. From comparisons to the saturated overlayer at 300 K, $\theta_{\text{O}} = 0.50$ ML after this exposure. Panel (a) shows θ_{O} , as measured with specular He scattering (solid line) and θ_{O} calculated from measured O_2 desorption intensity data (dashed line) (see panel (c)). Panel (b) shows the change in θ_{O} calculated from specular He scattering data (panel (a), solid line). Panel (c) shows the simultaneously measured O_2 desorption intensity. Comparisons of panel (a) solid and dotted lines indicate that the specular He scattering measurements of θ_{O} at $T_{\text{S}} > 625$ K are accurate at $\theta_{\text{O}} < 0.25$ ML.

θ_{O} , as measured with He reflectivity, and the simultaneously measured O_2 TPD (measured with the RGA). By comparing θ_{O} calculated from the He reflectivity measurements (Figure 6a) to θ_{O} calculated from the O_2 TPD measurement (Figure 6c), we see that both measurements indicate the same θ_{O} for $\theta_{\text{O}} < 0.25$. As noted above, the ordering of the O overlayer at $\theta_{\text{O}} > 0.25$ makes the calibration of the He reflectivity measurements for $T_{\text{S}} > 625$ K unreliable. We reiterate that the He reflectivity calibration of θ_{O} is reliable for $\theta_{\text{O}} < 0.15$ at all measured T_{S} .

In order to determine what the relative surface and subsurface concentrations of O are during a TPD measurement, we deposited 0.50 ML of O into the subsurface region by exposing the 650 K surface to a 1 ML/s 83 meV O_2 beam for 50 min. The surface concentration of O, as previously mentioned, was

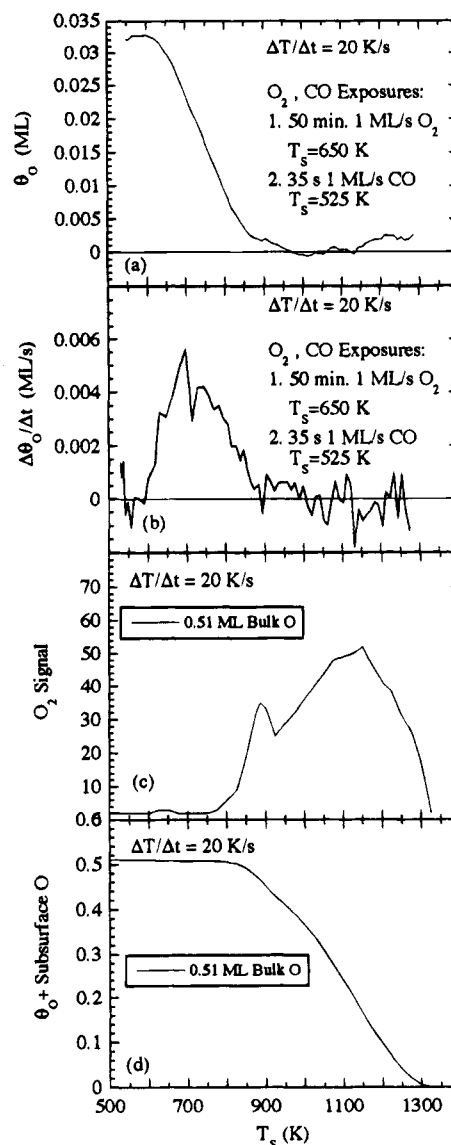


Figure 7. Concurrent O coverage and O_2 desorption measurement for subsurface O/Rh(111). Shown are measurements of θ_{O} and O_2 desorption made while heating Rh(111) which had been exposed to a 1 ML/s 63 meV O_2 beam at $T_{\text{S}} = 650$ K for 50 min. and then subsequently to a 1 ML/s 63 meV CO beam at $T_{\text{S}} = 525$ K for 35 s. The types of measurements shown are identical to those in Figure 6. As indicated in panel (a), $\theta_{\text{O}} = 0.033$ after the initial treatment (as measured with time-resolved specular He scattering). As the crystal is heated, the measurable θ_{O} drops to near zero at $T_{\text{S}} = 900$ K. Comparisons of panel (c), which indicates the rate of O_2 desorption, to panel (b), which shows the decrease in θ_{O} ($\Delta\theta_{\text{O}}/\Delta t$), indicate no relationship between O_2 desorption and $\Delta\theta_{\text{O}}/\Delta t$. Note that shape and intensity of the O_2 TPD in panel (c) is similar to the TPD for desorption of the known 0.50 ML saturated (2×2) O/Rh(111) overlayer (Figure 6c). Since the measurable surface coverage does not exceed 0.033 ML, we conclude that the O_2 originated in the subsurface region or bulk. With almost no measurable θ_{O} , the shape of the panel (c) O_2 TPD cannot be explained by a second-order desorption model which relates the shape to the changes in θ_{O} .

0.50 ML during this deposition. After this deposition, we reacted off most of the surface O (except for 0.035 ML) with CO at $T_{\text{S}} = 525$ K. We then proceeded with a TPD experiment, monitoring θ_{O} with He reflectivity and desorbing O_2 with the RGA (Figure 7). One remarkable result of this experiment is that, although 0.50 ML of O is depleted and desorbed from the subsurface region, θ_{O} never exceeds 0.035 ML.

By comparing the TPD from the subsurface O experiment (Figure 7c) to that of the surface O experiment (Figure 6c), we

note that there is a similarly shaped TPD curve for both experiments. The shapes of these curves result from the change in desorption rates as T_s increases and θ_0 decreases. Normally, the rate expression used for recombinative desorption considers only the change in surface coverage and the change in temperature in the rate expression

$$\frac{d\theta}{dt} = -k_{SO}[T_s(t)]\theta^2 = -\nu_{SO} \exp\left\{\frac{-E_a}{k_b[T_s(0) + (\Delta T/\Delta t)t]}\right\}\theta^2 \quad (1)$$

Two factors to consider with this approach are the probability that species will interact on the surface and changes in the activation energy due to interadsorbate interactions.

Initially, we assumed the shapes of the TPD curves were determined only by interactions between surface O species (eq 1). As indicated by the 650 K width of the TPD peaks (Figures 6c and 7c), the O₂ desorption rates vary by several orders of magnitude during O₂ desorption. Model TPD curves that assume constant activation energy, in which the desorption rate was proportional to θ_0^2 , could not account for these widths. Model TPD curves which assume a constant pre-exponential and an activation energy which increases monotonically with surface coverage could only account for the widths of the surface oxygen desorption TPDs (Figure 6c). Since θ_0 for the subsurface O TPD (Figure 7c) was at least an order of magnitude lower than θ_0 for the surface O TPD, we would expect that the desorption rates would be much slower and that the desorption peaks would shift to a much higher temperature. We observed, however, that the TPD curves in Figures 6c and 7c are essentially identical, indicating that, as a function of time and temperature, the O₂ desorption rates for both of these experiments were nearly identical.

Since identical heating rates and identical initial O concentrations for both experiments resulted in nearly identical desorption rates, we believe that the O₂ desorption rates were determined by the total concentration (subsurface plus surface) of O. If we integrate the peak areas, we see that the comparative total O concentrations are nearly the same at a given temperature on the TPD curves (see Figures 6a, dashed line, and 7d). We see from the TPD results that, at a given T_s , the desorption rates are nearly the same, regardless of surface coverage. The desorption profile and thus the desorption rates must therefore depend on the total concentration of O, regardless of whether this is a surface or subsurface species. One possibility is that the surface O on the subsurface O/Rh(111) islands and thus has a higher effective concentration as it desorbs. However, the degree to which the two TPD curves match indicates that the shape of the TPD curve depends primarily on the total number of O–O interactions between surface species and between surface and subsurface species; island formation is not the primary cause of this observation.

4. Steady State θ_0 Measurements. The equilibrium concentrations of surface O in the presence of subsurface O indicate the difference in chemical potential between the two species. The four processes which determine the surface and subsurface concentrations are adsorption, desorption, diffusion or absorption into the bulk and segregation from the bulk. At equilibrium

$$d\theta/dt = (\text{rate of adsorption}) + (\text{rate of segregation}) - (\text{rate of absorption}) - (\text{rate of desorption}) = 0 \quad (2)$$

If T_s and the O₂ pressure are low enough, the desorption and adsorption rates become much slower than the absorption and segregation rates:

$$d\theta/dt = (\text{rate of segregation}) - (\text{rate of absorption}) = 0 \quad (3)$$

Thus, the equilibrium concentrations of surface and subsurface O are determined only by segregation and absorption. In order to find coverage and temperature regimes for which such an equilibrium existed, we explored the response of the surface–subsurface system to the removal of surface O.

From a series of measurements, we determined that the maximum subsurface deposition rate occurs at $T_s = 650$ K for a 88 meV 1 ± 0.2 ML/s O₂ beam. O₂ desorption occurs for $T_s > 650$ K, but not for $T_s < 625$ K. 0.50 ML surface and 0.5 ML subsurface O was deposited by exposing the Rh(111) surface to the O₂ beam for 50 min (see Figure 5). This initial surface concentration was observed to decrease over a period of hours at $500 < T_s < 600$ K, indicating that the relaxation of the system to equilibrium is very slow (subsequent TPDs indicate that O did not desorb or react with background gases, but migrated into the bulk). In order to increase the rate of relaxation, the surface O was reacted off as CO₂ at $T_s = 525$ K with a 35 s exposure to a 88 meV 1 ± 0.2 ML/s CO beam (see Figure 5). After this treatment, $\theta_0 = 0.035$ ML, and the subsurface O concentration = 0.5 ML. CO exposures > 35 s and < 100 s, for which the surface O concentration was still ~ 0.035 ML, resulted in the depletion of subsurface O down to 0.25 ML (see Figure 5). CO exposures > 100 s, which resulted in subsurface O concentrations less than 0.2 ML, produced a surface O concentration < 0.033 ML. CO exposures < 33 s left an initial $\theta_0 > 0.035$ ML (see Figure 5), and θ_0 was observed to decrease over a period of 1 h down to $\theta_0 = 0.035$ ML. This indicates that 0.035 ML is the equilibrium θ_0 at 525 K. At a given constant T_s and θ_0 , the only changing quantity is subsurface concentration of O. Since θ_0 is constant for subsurface O concentrations (C_0) between 0.5 and 0.25 ML at the given T_s , we conclude (see eq 3) that both absorption and segregation rates are equal for $0.25 \text{ ML} < C_0 < 0.50 \text{ ML}$. Assuming the absorption rate depends primarily on the surface coverage, which is constant, the segregation rate is constant, and thus segregation is a zero-order process for $0.25 \text{ ML} < C_0 < 0.50 \text{ ML}$.

We determined the equilibrium surface concentration of O with 0.5 ± 0.05 ML subsurface O for a range of temperatures. After depositing 0.5 ± 0.05 ML of subsurface O and reacting off surface O with CO at 525 K, we note that the surface O concentration equilibrates at $\theta_0 < 0.05$, measurable with He reflectivity. We measured the steady state θ_0 with He reflectivity for $T_s = 525$ –800 K (Figure 8). The subsurface O concentration changed by $< 10\%$ during these measurements. At higher temperatures, O desorption rates are too high to maintain a constant subsurface O concentration. From these measurements, we see that as T_s increases, θ_0 decreases. We note that we repeated this experiment for $C_0 < 0.5$ ML at several temperatures and observed identical θ_0 values.

The kinetic model we use to describe the steady state O concentration assumes no O₂ adsorption (O₂ pressures were $< 10^{-11}$ Torr), a temperature and subsurface concentration dependent O segregation rate, and temperature, surface coverage, and subsurface concentration dependent O absorption and desorption rates. At steady state

$$d\theta/dt = R_{\text{SEG}}(T_s, C_0) - K_{\text{ABS}}(T_s, C_0)\theta_0 - K_{\text{DES}}(T_s, C_0)\theta_0^2 = 0 \quad (4)$$

or

$$R_{\text{SEG}}(T_s, C_0) = K_{\text{ABS}}(T_s, C_0)\theta_0 + K_{\text{DES}}(T_s, C_0)\theta_0^2 \quad (5)$$

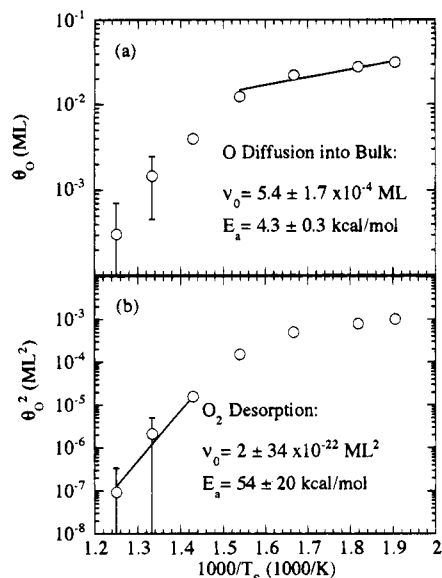


Figure 8. Arrhenius plots of steady state θ_O and θ_O^2 with 0.5 ML subsurface O. Shown here are Arrhenius plots of steady state (a) θ_O and (b) θ_O^2 for O/Rh(111) with a measured 0.5 ML of O (0.8×10^{15} O atoms/cm²) in the subsurface region. The steady state θ_O was measured with time resolved specular He scattering at $T_S = 525$ –800 K. A model for the observed data is proposed in the text. The observed trends in the data suggest that, for $T_S < 650$ K ($1000/T > 1.54$), the equilibrium surface coverage is dominated by the surface to subsurface diffusion process, with a measured $E_a = E_{\text{ABS}} - E_{\text{SEG}}$ (see text) of 4.3 ± 0.3 kcal/mol and that for $T_S > 650$ K ($1000/T < 1.54$) the equilibrium surface coverage is dominated by the second-order O₂ desorption process, with a measured $E_a = E_{\text{DES}} - E_{\text{SEG}}$ (see text) of 54 ± 20 kcal/mol.

$K_{\text{ABS}}(T_S, C_O)$ = the first-order absorption rate constant (we assume first-order absorption because in the low- θ_O limit and at elevated temperatures, O species are relatively dilute), $R_{\text{SEG}}(T_S, C_O)$ = the segregation rate (constant at a given T_S and $0.25 < C_O < 0.50$), and $K_{\text{DES}}(T_S)$ = the second-order O₂ desorption rate constant, with C_O = the subsurface O concentration. We assume an Arrhenius form for each of the rates and rate constants:

$$R_{\text{SEG}}(T_S, C_O) = \nu_{\text{SEG}}(C_O) \exp[-E_{\text{SEG}}(C_O)/k_b T_S] \quad (6)$$

$$K_{\text{ABS}}(T_S, C_O) = \nu_{\text{ABS}}(C_O) \exp[-E_{\text{ABS}}(C_O)/k_b T_S] \quad (7)$$

$$K_{\text{DES}}(T_S, C_O) = \nu_{\text{DES}}(C_O) \exp[-E_{\text{DES}}(C_O)/k_b T_S] \quad (8)$$

The notation $\nu_\alpha(C_O)$ does not imply the order of the rate, only that the rate depends in some (nonexplicit) way on C_O . In the low-temperature regime where absorption is much faster than desorption, the rate equation reduces to

$$\nu_{\text{SEG}}(C_O) \exp[-E_{\text{SEG}}(C_O)/k_b T_S] = \nu_{\text{ABS}}(C_O) \exp[-E_{\text{ABS}}(C_O)/k_b T_S] \theta_O \quad (9)$$

$$\theta_O = [\nu_{\text{SEG}}(C_O)/\nu_{\text{ABS}}(C_O)] \exp\{-[E_{\text{SEG}}(C_O) - E_{\text{ABS}}(C_O)]/k_b T_S\} \quad (10)$$

As we have mentioned, θ_O is independent of C_O for $0.25 \text{ ML} < C_O < 0.5 \text{ ML}$, which means that $\nu_{\text{SEG}}(C_O)/\nu_{\text{ABS}}(C_O)$ is constant. From Figure 8a, we determined $E_{\text{SEG}}(C_O) - E_{\text{ABS}}(C_O) = -4.3 \pm 0.3$ kcal/mol, indicating that the energy of adsorption is greater than the energy of absorption by 4.3 ± 0.3 kcal/mol. Also, $\nu_{\text{SEG}}(C_O)/\nu_{\text{ABS}}(C_O) = 5.4 \pm 1.7 \times 10^{-4} \text{ ML}$ for $C_O = 0.25$ –0.5 ML. At higher temperatures, O₂ desorption rates are

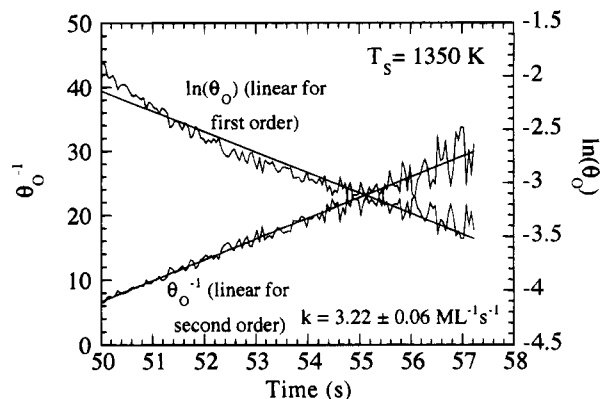


Figure 9. First- versus second-order kinetics for O₂ desorption. Shown are the isothermal θ_O^{-1} and $\ln(\theta_O)$ curves for O₂ desorbing from Rh(111) at $T_S = 1350$ K. θ_O was measured with time dependent specular He scattering. Since the plot of $\ln(\theta_O)$ shows clear deviation from a straight line, whereas θ_O^{-1} is fit well by a straight line, O₂ desorption in this regime ($\theta_O = 0.036$ –0.154) is probably a second-order process, $d\theta_O/dt = -k\theta_O^2$. The measured second-order rate constant $k = 3.22 \pm 0.06 \text{ ML}^{-1} \text{ s}^{-1}$ or $2.01 \pm 0.04 \times 10^{-15} \text{ cm}^2/\text{s}$.

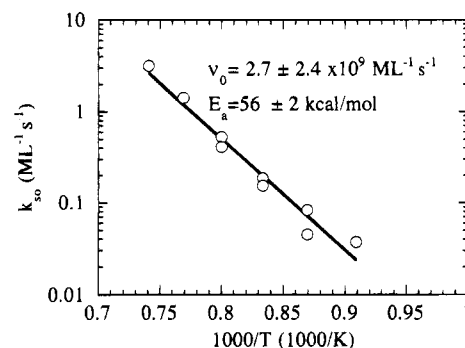


Figure 10. Arrhenius plot of isothermal O₂ desorption. Shown is an Arrhenius plot of the isothermal second-order O₂ desorption rates for $\theta_O = 0.02$ –0.20 and $T_S = 1100$ –1350. The desorption rates were measured using time dependent specular He scattering (see Figure 9). From the plot, $E_a = 56 \pm 2$ kcal/mol and $\nu_0 = 2.7 \pm 2.4 \times 10^9 \text{ ML}^{-1} \text{ s}^{-1}$ or $1.7 \pm 1.4 \times 10^{-6} \text{ cm}^2/\text{s}$.

much faster than absorption rates. The rate equation is

$$\nu_{\text{SEG}}(C_O) \exp[-E_{\text{SEG}}(C_O)/k_b T_S] = \nu_{\text{DES}}(C_O) \exp[-E_{\text{DES}}(C_O)/k_b T_S] \theta_O^2 \quad (11)$$

$$\theta_O^2 = [\nu_{\text{SEG}}(C_O)/\nu_{\text{DES}}(C_O)] \exp\{-[E_{\text{SEG}}(C_O) - E_{\text{DES}}(C_O)]/k_b T_S\} \quad (12)$$

From Figure 8b, we determined $E_{\text{SEG}}(C_O) - E_{\text{DES}}(C_O) = -54 \pm 20$ kcal/mol.

5. Low θ_O O₂ Desorption Kinetics. Using He scattering, we followed $\theta_O(t)$ as O desorbed. We note (Figure 9) that O desorption follows second-order desorption kinetics with a constant $k_{\text{so}}(T_S)$ for $T_S = 1350$ K and $\theta_O = 0.04$ –0.17 ML. At higher or lower coverages, the desorption rate appears to increase. The expected increase at higher coverages is due to the stronger O–O interaction energies. At lower coverages, the diffusion of O into the bulk competes with O desorption, causing O to disappear but not desorb at a higher rate. From an Arrhenius plot of the second-order desorption rates, $k_{\text{so}}(T_S)$ (Figure 10), we determined $\nu_{\text{so}} = 2.7 \pm 1.5 \times 10^9 \text{ ML}^{-1} \text{ s}^{-1}$ and $E_a = 56 \pm 2$ kcal/mol. This E_a agrees well with the E_a measured by Thiel et al. of 56 ± 2 kcal/mol.¹⁴

B. Surface to Bulk Diffusion Kinetics. 1. Using O₂. We compared the rates at which O₂, NO, and NO₂ deposit O into

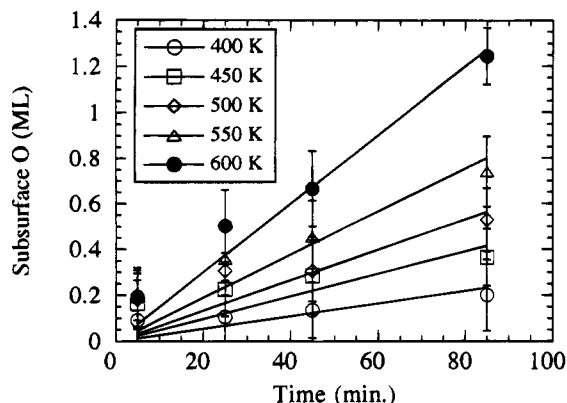


Figure 11. Isothermal deposition rates for subsurface O from O_2 dosing. Shown here is the measured amount of O in the subsurface region of Rh(111) for a 1 ± 0.2 ML/s 63 meV (room temperature) O_2 beam. The amount of O in the bulk was determined by thermal desorption of O_2 . The measured signal from surface O (0.5 ML) was used to normalize the data and was then subtracted from the total signal. The net subsurface or bulk O signal was determined, as indicated, for $T_s = 400$ – 600 K and for exposure times from 5 to 85 min. The data indicate that subsurface O deposition or diffusion (up to 1.2 ML) is a linear function of time. The diffusion rates, indicated by the solid lines, are shown in Table 1.

TABLE 1: O Absorption Rates for Rh(111) Exposed to 1 ± 0.2 ML/s 63 meV O_2

temperature (K)	diffusion rate (ML/min)	error diffusion rate (ML/min)
400.00	0.0027	0.0015
450.00	0.0049	0.0013
500.00	0.0066	0.0014
550.00	0.0094	0.0016
600.00	0.0150	0.0013

the subsurface region by dosing the Rh(111) surface with each oxidant and desorbing all adsorbed and absorbed O. From our previous measurements, we assumed that the total surface concentration of O for these measurements remained at 0.50 ML. The measured 0.50 ML surface O signal was then subtracted from the total desorbed O_2 signal (flux density corrected) to yield a subsurface O signal. For an 88 meV 1 ± 0.2 ML/s O_2 beam, we measured subsurface O deposition yields at 400, 450, 500, 550, and 600 K (Figure 11). O_2 , as we have previously shown²⁰ (contrary to previous studies²⁵), adsorbs with second-order kinetics. These kinetics imply that two adjacent empty sites^{26–29} are necessary for adsorption. We note that the bulk O deposit yields are nearly proportional to O_2 exposure times, indicating a constant deposition rate for the measured constant $\theta_O = 0.5$ ML. We calculated deposition rates (Table 1) and determined Arrhenius parameters for the deposition of O into Rh(111) (Figure 12). We note that the E_a of 4.3 ± 0.7 kcal/mol is within experimental error of $E_{ABS} - E_{SEG} = 4.3 \pm 0.3$ kcal/mol measured for the steady state experiment (Figure 8a). This indicates that the energy required to go from the adsorbed state to the absorbed state is the actual difference in energy between these two states (little additional activation energy is required).

2. Using NO. We used an 88 meV 1 ± 0.2 ML/s NO beam to deposit subsurface O into 525 K Rh(111). We note that the initial diffusion rate (Figure 13) of 0.022 ± 0.004 ML/min is 2.5 times faster than the uptake (calculated from Figure 12 data) of 0.0088 ML/s for O_2 under the same conditions. We also note that we do see some evidence for a change in the absorption kinetics at $C_O \sim 0.85$. The uptake rate starts to slow. The possible reasons for the differences in subsurface O deposition between O_2 and NO relate to the adsorption of O_2 and NO at

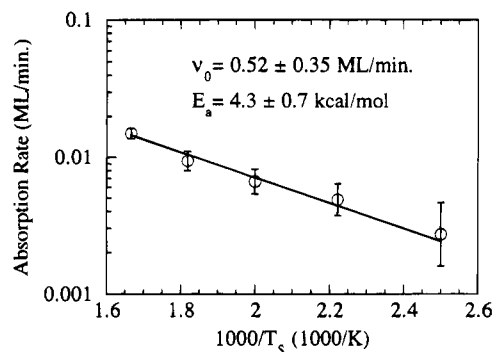


Figure 12. Arrhenius plot of surface to subsurface O absorption rate from O_2 dosing. Shown here is the Arrhenius plot of the diffusion rates from Figure 11. From the plot, $E_a = 4.3 \pm 0.7$ kcal/mol and a $v_0 = 0.52 \pm 0.35$ ML/min.

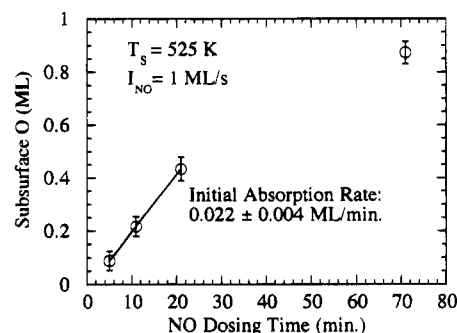


Figure 13. Deposition rate of subsurface O from NO dosing. The 525 K Rh(111) surface was exposed to a 1 ML/s NO beam at the exposure times indicated, and subsequent thermal desorptions of absorbed and adsorbed O (as O_2) were used to assess the net O absorbed into the bulk. Compared to results for O_2 exposures at similar intensities (see Figure 11, 500, 550 K results), this figure shows that NO deposits O much faster than O_2 . From Figure 12, the calculated absorption rate for a similar O_2 beam at $T_s = 525$ K is 0.0088 ML/s, compared to the measured 0.022 ± 0.004 ML/s rate for absorption from NO. Note that the 71 min NO exposure O absorption is asymptotically approaching a saturation value of ~ 1 ML, while the 85 min O_2 exposure O absorption is still increasing linearly.

near saturation θ_O . In comparison with O_2 adsorption on 0.5 ML of O, there is both a higher effective pressure of NO for the same incident flux and, more importantly, a larger chemical driving force due to the coadsorption of both O and NO on the Rh(111) surface.^{2,19,30} Since O_2 adsorbs dissociatively and requires two adjacent empty 3-fold hollow sites, O_2 cannot adsorb at saturation θ_O . However, NO adsorbs molecularly and will coadsorb on top sites while O is adsorbed at 3-fold hollow sites,^{2,19,30} thus allowing immediate deposition of O when a surface O absorbs into the subsurface region. So the rate at which an absorbed O is replaced increases with NO, thus keeping the surface concentration slightly higher than with O_2 dosing. In addition, the presence of adsorbed NO, which has been shown to have a repulsive interaction with adsorbed O,^{2,19,30} exerts an extra chemical driving force due to NO–O repulsion, which can increase O absorption rates by driving the surface O species into the bulk.

3. Using NO_2 . Using an uncalibrated room temperature beam of unmixed NO_2 , we deposited subsurface O into Rh(111). We place an upper limit on the NO_2 flux at 1 ML/s, although the chamber pressure rise indicated a flux nearer to 0.20 ML/s. During the O deposition with NO_2 , we measured only mass 30 (NO) and mass 46 (NO_2) species leaving the surface. The TPD from NO_2 deposition (Figure 14) shows an additional peak (~ 800 K) at O deposition yields not accessed with O_2 or NO. The initial O absorption rate from NO_2 (Figure 15) was >0.95

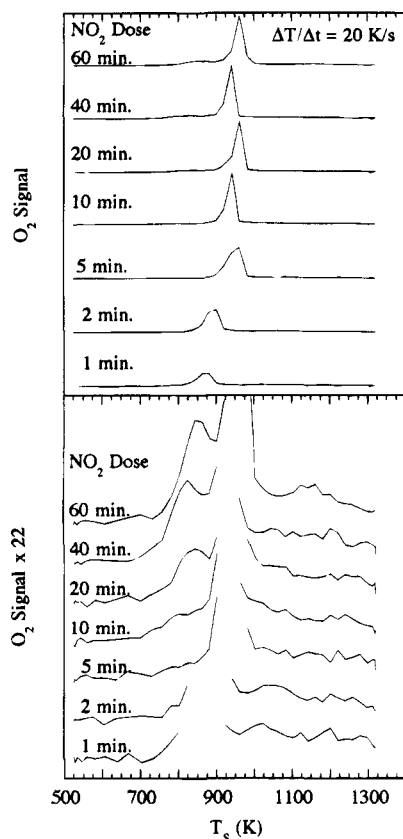


Figure 14. O_2 TPDs after exposure to NO_2 . Shown are the O_2 TPDs from exposure to NO_2 . The top panel is full scale, and the bottom panel is expanded by a factor of 20. There are three distinct features in these TPDs. The sharp peak, centered at 850 K at short exposures (top panel), shifts to 975 K at longer exposures. This peak is the same peak that appears at 750–800 K in Figures 3, 4, and 6c. The broad peak (bottom panel), centered at 1150 K, appears to saturate at short exposures and also appears (slightly shifted) in Figures 3, 4, and 6c. An additional sharp peak centered at $T_s = 825$ K appears (bottom panel) only for exposures longer than 10 min. This peak was not observed in any O_2 TPDs from NO or O_2 dosing.

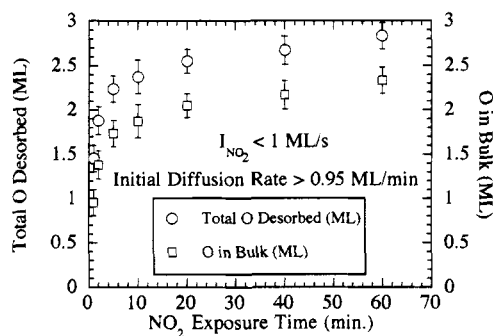


Figure 15. Deposition rate of subsurface O from NO_2 dosing. The 525 K Rh(111) surface was exposed to a constant intensity NO_2 beam at the exposure times indicated, and subsequent thermal desorptions of adsorbed and adsorbed O (as O_2) were used to assess the total O desorbed and the net O absorbed into the bulk (the maximum surface coverage is 0.5 ML). We note that the subsurface O concentration rapidly approaches 1.5 ML then slowly approaches an apparent saturation value of ~ 2.5 ML. The initial O absorption rate from NO_2 was >0.95 ML/min, 43 times faster than absorption from NO and 108 times faster than absorption from O_2 .

ML/min, at least 43 times as fast as the deposition from NO and 108 times as fast as the deposition from O_2 . Since $\theta_{O-(max)} = 0.5$ ML for O_2 adsorption, and the coverage created by NO_2 dosing can only be at most 1 ML (due to the size of adsorbed O), this effect cannot be only a coverage effect, but

must also be due to an extra chemical driving force present with NO_2 . This effect can be understood by considering the chemistry of NO_2 on other surfaces. On Pt(111) surfaces, a sticking coefficient of unity has been measured for low-temperature NO_2 adsorption,³¹ even at $\theta_O = 0.75$ ML, implying that NO_2 adsorption is relatively insensitive to θ_O . EELS measurements indicate that NO_2 adsorbs on bridge-bonded sites in a configuration which allows dissociative adsorption of O and NO when an adjacent O adsorption site is free. If we assume that the O saturates on the surface at 0.50 ML, the subsurface O appears to saturate near 2.25 ML, although we cannot conclusively rule out the possibility that $\theta_O > 0.50$ ML for NO_2 dosing. This saturation behavior is probably due to a change of absorption kinetics as O saturates the subsurface region layer by layer. Several researchers have proposed a near surface stoichiometry of Rh_2O_3 when O is deposited from high (>1 Torr) pressures of O_2 .^{11,13} Our data indicate that $O/Rh > 1.5$ in the near surface region. From this, we infer that either the 2:3 stoichiometry is exceeded or O penetrates several layers into the Rh(111) surface.

IV. Discussion

A. Effects of Subsurface O on Catalytic Reactions.

Subsurface O can affect the surface chemical reactions in one of two ways. The abundant subsurface O can serve as a O reservoir for surface reactions. The presence of subsurface O can also affect the bonding and reaction energetics. For O on Rh(111), subsurface O segregation contributes to surface O coverage only at very low (<0.05 ML) O coverages. From our titration measurements with CO, we know that CO oxidation at these coverages is not limited by the segregation rate but by the surface reaction rate. Thus, in the absence of a gas phase oxidant (O_2 , NO), CO oxidation will occur as long as there is a supply of subsurface O. In general, the presence of an electron withdrawing coadsorbate, such as $S^{32,33}$ and Se,³² will decrease the binding energy of CO, while electron-donating coadsorbates such as Na,^{34,35} K,^{34–36} and Cs^{34–36} will increase the binding energies of both CO and O. As shown previously, the presence of subsurface O will also lower the activation energy for CO oxidation at higher O coverages. The shift in the O_2 desorption peak position toward lower temperatures as O coverages increase¹⁰ is also consistent with a lowering of the activation energy for O_2 desorption. Thus, on Rh(111), subsurface O can both supply O for surface reactions and modify the reaction rates by decreasing the binding energies of the adsorbates.

B. Effects of Subsurface O on Surface O. For the case of O_2 desorption from Rh(111), the subsurface O can serve as a reservoir to replace desorbing O and modify the O-surface binding energies. When the total O, adsorbed and adsorbed, is less than 0.5 ML, the comparison of O_2 desorption with surface coverage indicated that the primary effect of subsurface O was a modification of the binding energies. Since O is strongly electrophilic, regardless of whether it is on the surface or in the subsurface region, the available electron density for surface bonding should decrease in proportion to the total number of surface and near surface O. A decrease in bond energy for O will decrease the activation energy necessary to desorb O_2 . The desorption rate, we conclude, was thus determined primarily by the through-bond interactions between adsorbed and adsorbed O species.

However, in the case of O_2 desorption with total O >1 ML, we note that there is an excess of O desorbing at the lower temperature (~ 800 K) peak. Here the surface coverage was 0.5 ML, many times the 0.035 ML equilibrium surface coverage we observed when we depleted the surface coverage of O with

CO. We note that there is no correlation between the specular He scattering measurement of θ_O and the desorbing O_2 signal. This means that O desorbing from the surface is replaced with O segregating from the bulk or that O from the bulk segregates to the surface and is immediately desorbed. Either way, our results imply that segregation from the bulk at $T_S > 700$ K, $C_O = 0.5$ ML, and $\theta_O = 0.5$ ML is faster than absorption or desorption for these same conditions.

V. Conclusion

We have conclusively proven the existence of a subsurface O species which grows in from adsorbed O on Rh(111) at $T_S > 375$ K. The subsurface O will segregate to and desorb from the Rh(111) surface at $T_S > 650$ K. The rate of subsurface O deposition varies with the source of O, with the rate for $NO_2 \gg NO > O_2$. From our measurements, we have determined the relative energetics for absorption, segregation, and desorption. Arrhenius analysis of the rates of absorption for O_2 shows that $E_a = 4.3 \pm 0.7$ kcal/mol for absorption. An analysis of the steady state surface O coverages with 0.5 ML O subsurface indicates a difference in enthalpy of 4.3 ± 0.3 kcal/mol between the surface and subsurface O and that the difference between the segregation activation energy and the desorption activation energy is 54 ± 20 kcal/mol. In addition, Arrhenius analysis of isothermal O_2 desorption measurements for $\theta_O < 0.15$ show that $E_a = 56 \pm 2$ kcal/mol for O_2 desorption. The shape of O_2 desorption peaks at total O ~ 0.5 ML is independent of the source of O, surface or subsurface. Rate analysis indicates that the intermolecular interactions between coadsorbed O species are approximately the same magnitude as the interaction between adsorbed and absorbed O species.

Acknowledgment. The authors wish to thank Dr. Kevin Gibson and Jennifer Colonell for their helpful suggestions. Acknowledgment is made to the donors of The Petroleum Research Fund, administered by the ACS, for partial support of this research. Additional support from the NSF Materials Research Science and Engineering Center at The University of Chicago is also gratefully acknowledged.

References and Notes

- (1) Matsushima, T. *Surf. Sci.* **1985**, *157*, 297.
- (2) Root, T. W.; Fisher, G. B.; Schmidt, L. D. *J. Chem. Phys.* **1986**, *85*, 4679.
- (3) Parker, D. H.; Bartram, M. E.; Koel, B. E. *Surf. Sci.* **1989**, *217*, 489.
- (4) Bartram, M. E.; Windham, R. G.; Koel, B. E. *Surf. Sci.* **1987**, *184*, 57.
- (5) Parker, D. H.; Koel, B. E. *J. Vac. Sci. Tech. A* **1990**, *8*, 2585.
- (6) Wickham, D. T.; Banse, B. A.; Koel, B. E. *Surf. Sci.* **1991**, *243*, 83.
- (7) Banse, A.; Koel, B. E. *Surf. Sci.* **1990**, *232*, 275.
- (8) Malik, I. J.; Hrbek, J. *J. Vac. Sci. Tech. A* **1992**, *10*, 2565.
- (9) Xu, X.; Friend, C. *J. Am. Chem. Soc.* **1991**, *113*, 6779.
- (10) Root, T. W.; Schmidt, L. D.; Fisher, G. B. *Surf. Sci.* **1983**, *134*, 30.
- (11) Logan, A. D.; Datye, A. K.; Houston, J. E. *Surf. Sci.* **1991**, *245*, 280.
- (12) Derry, G. N.; Ross, P. N. *Surf. Sci.* **1984**, *140*, 165.
- (13) Castner, D. G.; Somorjai, G. A. *Appl. Surf. Sci.* **1980**, *6*, 29.
- (14) Thiel, P. A.; Yates, J. T., Jr.; Weinberg, W. H. *Surf. Sci.* **1979**, *82*, 22.
- (15) Segner, J.; Campbell, C. T.; Doyen, G.; Ertl, G. *Surf. Sci.* **1984**, *138*, 505.
- (16) Bassett, M. R.; Imbihl, R. *J. Phys. Chem.* **1990**, *93*, 811.
- (17) Brown, L. S.; Sibener, S. J. *J. Chem. Phys.* **1988**, *89*, 1163. Gibson, K. D.; Sibener, S. J. *J. Chem. Phys.* **1988**, *88*, 791.
- (18) Peterlinz, K. A.; Curtiss, T. J.; Sibener, S. J. *J. Chem. Phys.* **1991**, *95*, 6972.
- (19) Castner, D. G.; Sexton, B. A.; Somorjai, G. A. *Surf. Sci.* **1978**, *71*, 519.
- (20) Peterlinz, K. A.; Sibener, S. J. To be published.
- (21) Neuhaus, D.; Joo, F.; Feuerbacher, B. *Phys. Rev. Lett.* **1987**, *58*, 694.
- (22) Yu, C.-F.; Ph.D. Dissertation, University of Chicago, March, 1984.
- (23) Lapujoulade, J.; Perreau, J.; Kara, A. *Surf. Sci.* **1983**, *129*, 59.
- (24) Armand, G.; Lapujoulade, J.; Lejay, Y. *Surf. Sci.* **1977**, *63*, 143.
- (25) Yates, J. T., Jr.; Thiel, P. A.; Weinberg, W. H. *Surf. Sci.* **1979**, *82*, 45.
- (26) Wong, P. C.; Hui, K. C.; Zhou, M. Y.; Mitchell, K. A. *R. Surf. Sci.* **1986**, *165*, L21.
- (27) Winograd, N.; Kobrin, P. H.; Schick, G. A.; Singh, J.; Baxter, J. P.; Garrison, B. J. *Surf. Sci.* **1986**, *176*, L817.
- (28) Reimann, C. T.; El-Maazawi, M.; Walzl, K.; Garrison, B. J.; Winograd, N.; Deaven, D. M. *J. Chem. Phys.* **1989**, *90*, 2027.
- (29) Singh, J.; Reimann, C. T.; Baxter, J. P.; Schick, G. A.; Kobrin, P. H.; Garrison, B. J. *J. Vac. Sci. Tech. A* **1987**, *5*, 1191.
- (30) Bugyi, L.; Kiss, J.; Révész, K.; Somolymosi, F. *Surf. Sci.* **1990**, *223*, 1.
- (31) Bartram, M. E.; Windham, R. G.; Koel, B. E. *Langmuir* **1988**, *4*, 240.
- (32) Kiskinova, M. P.; Szabò, A.; Yates, J. T., Jr. *Surf. Sci.* **1990**, *226*, 237.
- (33) Kiskinova, M.; Szabò, A.; Yates, J. T., Jr. *J. Chem. Phys.* **1988**, *89*, 7599.
- (34) Surnev, L.; Rangelov, G.; Kiskinova, M. *Surf. Sci.* **1987**, *179*, 283.
- (35) Kiskinova, M. *J. Vac. Sci. Tech. A* **1987**, *5*, 852.
- (36) Kiskinova, M.; Tikhov, M. *Surf. Sci.* **1988**, *194*, 379.